

Journal of Biomedical Optics

SPIEDigitalLibrary.org/jbo

Dynamic optical coherence tomography measurements of elastic wave propagation in tissue-mimicking phantoms and mouse cornea *in vivo*

Jiasong Li
Shang Wang
Ravi Kiran Manapuram
Manmohan Singh
Flores M. Menodiado
Salavat Aglyamov
Stanislav Emelianov
Michael D. Twa
Kirill V. Larin

Dynamic optical coherence tomography measurements of elastic wave propagation in tissue-mimicking phantoms and mouse cornea *in vivo*

Jiasong Li,^a Shang Wang,^a Ravi Kiran Manapuram,^b Manmohan Singh,^a Floredes M. Menodiado,^a Salavat Aglyamov,^b Stanislav Emelianov,^b Michael D. Twa,^c and Kirill V. Larin^{a,d,e}

^aUniversity of Houston, Department of Biomedical Engineering, 4800 Calhoun Road, Houston, Texas 77004

^bThe University of Texas at Austin, Department of Biomedical Engineering, 107 W. Dean Keeton Street Stop C0800, Austin, Texas 78712

^cUniversity of Houston, College of Optometry, 505 J. Davis Armistead Building, Houston, Texas 77204-2020

^dUniversity of Houston, Department of Mechanical Engineering, 4800 Calhoun Road, Houston, Texas 77004

^eBaylor College of Medicine, Department of Molecular Physiology and Biophysics, One Baylor Plaza, Houston, Texas 77030

Abstract. We demonstrate the use of phase-stabilized swept-source optical coherence tomography to assess the propagation of low-amplitude (micron-level) waves induced by a focused air-pulse system in tissue-mimicking phantoms, a contact lens, a silicone eye model, and the mouse cornea *in vivo*. The results show that the wave velocity can be quantified from the analysis of wave propagation, thereby enabling the estimation of the sample elasticity using the model of surface wave propagation for the tissue-mimicking phantoms. This noninvasive, non-contact measurement technique involves low-force methods of tissue excitation that can be potentially used to assess the biomechanical properties of ocular and other delicate tissues *in vivo*. © 2013 Society of Photo-Optical Instrumentation Engineers (SPIE) [DOI: 10.1117/1.JBO.18.12.121503]

Keywords: optical coherence tomography; surface elastic wave; mouse cornea; air puff; Young's modulus; noninvasive detection.

Paper 130361SSPRR received May 22, 2013; revised manuscript received Aug. 31, 2013; accepted for publication Sep. 6, 2013; published online Oct. 2, 2013.

1 Introduction

The biomechanical characteristics of ocular tissues can have a profound influence on the health, structural integrity, and normal function of the eye.^{1,2} As a critical component of normal vision, the cornea provides approximately two-thirds of the optical refracting power of the eye. Several diseases, such as axial elongation in myopia, pathological deformation in keratoconus, and iatrogenic keratoectasia following corneal refractive surgery can alter biomechanical properties of the cornea and lead to poor vision and even blindness.³ Thus, the study of the biomechanical properties of cornea can help to detect and diagnose the severity of certain ocular diseases and complement the structural imaging of the eye.

Most of the previous attempts to measure tissue elasticity, compressibility, and shear forces have relied on inducing an excitation and measuring the tissue's response to that excitation. The excitation can be induced in many ways, e.g., with mechanical force,^{4,5} acoustic radiation force,⁶ or by using a pulsed laser.⁷ Several elasticity imaging modalities, which combine different methods of excitation and measurement, have been proposed to measure soft tissue elastic properties, such as magnetic resonance elastography,^{5,8-10} ultrasound elastography,^{11,12} acoustic radiation force imaging,^{13,14} dynamic corneal imaging,¹⁵ and supersonic shear imaging.^{6,16,17} However, all of these methods require significant amplitude of tissue stimulation in order to produce a measurable signal, which may not be applicable for delicate tissues such as the eye during *in vivo* studies. Holographic imaging has been used to study the elasticity of

soft materials and tissues successfully. However, the motion of tissue may reduce the accuracy of this method in monitoring the wave propagation. This makes it difficult to be applied to the cornea *in vivo* study.¹⁸

Brillouin microscopy is another method that has been successfully used to achieve the depth-dependent biomechanical properties in the human cornea *in vivo*.¹⁹ It has the ability to provide three-dimensional (3-D) elasticity maps of tissue with high-spatial resolution.²⁰ This technique relies on Brillouin scattering, which does not need excitation of tissue deformation. The interpretation of the signals produced by this method and their relation to familiar mechanical parameters, e.g., Young's modulus is an open question.

The ocular response analyzer (ORA) and the CorVis are two approaches currently available for clinical evaluation of the biomechanical properties of cornea.²¹⁻²³ Both are marketed as devices for the measurement of intraocular pressure and are based on a large amplitude of air pulse that displaces large volumes of tissue. This introduces a significant nonlinear component to the measured properties. Moreover, results from recent clinical studies demonstrated the inability of ORA to identify keratoconus-suspect corneas.²³

Optical coherence tomography (OCT) is an emerging technique that enables noninvasive imaging of ocular tissues with both high spatial and temporal resolutions.^{18,24,25} It has been demonstrated that phase-stabilized OCT is capable of resolving the tissue displacement in nanometer scale²⁶ as well as quantifying the propagation of low amplitude mechanical waves in tissue.²⁷⁻³⁴ The surface wave method, which relates the Young's modulus of sample to the propagation velocity of

Address all correspondence to: Kirill V. Larin, University of Houston, Department of Biomedical Engineering, 4800 Calhoun Road, Houston, Texas 77004. Tel: (832)842-8834; Fax: (713)743-0226; E-mail: klarin@central.uh.edu

surface wave, has been widely used for the quantification of sample elasticity.¹⁶ Recently, OCT combined with an air puff system has been employed to measure the characteristics of corneal deformation *in vivo*.³⁴ Here, we demonstrate the use of phase-stabilized swept source OCT (PhS-SSOCT) to assess the waves induced by a focused air-pulse system in tissue-mimicking phantoms and in corneal tissue *in vivo*. By using this non-contact excitation source, our results show that the PhS-SSOCT system is capable of measuring low-amplitude waves in the scale of microns. Therefore, the combination of air-pulse excitation and PhS-SSOCT measurement is potentially useful for studying the biomechanical properties of ocular tissues *in vivo*. To our best knowledge, this is the first study demonstrating the possibility of completely noninvasive exciting and quantifying the surface waves *in vivo* using optical coherence elastography.

2 Experimental Methods

2.1 System Setup

Elastic waves are induced in the sample using a home-built air-pulse delivery system that produces a focused air stream with a duration of ≤ 1 ms. The spatial-temporal profile of the air pulse is characterized as a Gaussian shape. Briefly, the system employs an air gate and a control unit to provide the short-duration air puff. An extra channel for signal output from the control unit allows proper synchronization with the PhS-SSOCT measurement system. The air source pressure can be obtained from a pressure gauge, and the output of the air-pulse system is through a cannula port with a flat edge and the diameter of ~ 150 μm . The localized air-pulse excitation can be precisely positioned through a 3-D linear micrometer stage. This excitation system can be treated as a noncontact stimulation method.

A PhS-SSOCT imaging system is combined with this air-pulse system to detect elastic waves in the sample. The schematic of the experimental setup for the *in vivo* study of mouse cornea is shown in Fig. 1. Briefly, the PhS-SSOCT

system is composed of a broadband swept laser source (HSL2000, Santec, Inc., Torrance, California) with the central wavelength of 1310 nm, the bandwidth of ~ 150 nm, the scan rate of 30 kHz, and the output power of ~ 36 mW. Interference is produced by the light coming from the sample and reference paths using a Mach-Zehnder interferometer and the fringes are detected by a balanced photodetector. A fiber Bragg grating is used for triggering the A-scan acquisition. The details of the system description can be found in our previous work.^{29,35,36} The axial resolution of the system is ~ 11 μm , and the phase stability of the system is experimentally measured to be ~ 16 mrad (corresponding to ~ 3.3 nm displacement in air). The air-pulse system generates a transistor-transistor logic signal which is recorded by the analog-to-digital converter for synchronization.

2.2 Experimental Materials

In order to simulate soft tissue samples of controlled stiffness, gelatin phantoms of five different concentrations (8%, 10%, 12%, 14% and 16% w/w) were prepared. Gelatin powder (PB Leiner, 250 Bloom/8 Mesh) was mixed with distilled water at 60°C until all granules were dissolved. Special care was taken while stirring the mixture to avoid the formation of air bubbles. The mixture was poured into a round mold to create a disk of ~ 11 -mm-thick and ~ 33.5 mm in diameter [Fig. 2(a)] and cooled down in a refrigerator for 30 min ($\sim 10^\circ\text{C}$).³⁷ The solidified gel formed a solid slab that served as a tissue-mimicking sample.

The contact lens used was a commercially available lens (Bausch & Lomb, Slisoft + 12.00D, 100% Silicone) that has a convex-concave shape similar to the cornea and has homogeneous optical and mechanical properties. During the experiments, the contact lens was fixed on a flat plate, and the space between the contact lens and the plate was filled with $1\times$ phosphate-buffered saline simulating the aqueous humor in a second experiment.

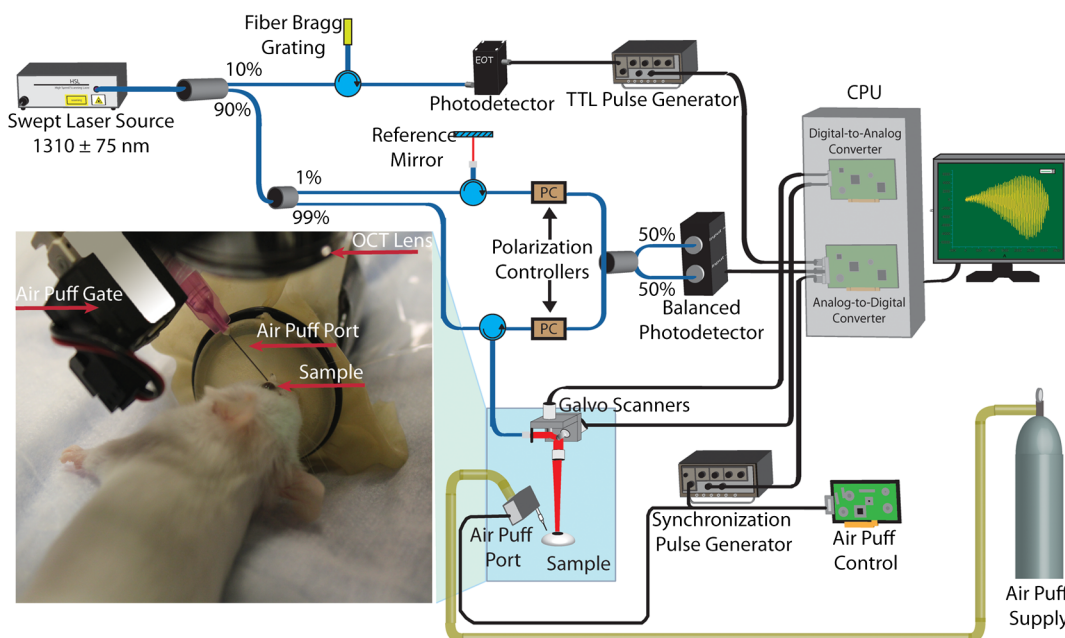


Fig. 1 Schematic of the system setup used in the *in vivo* study of the mouse cornea.

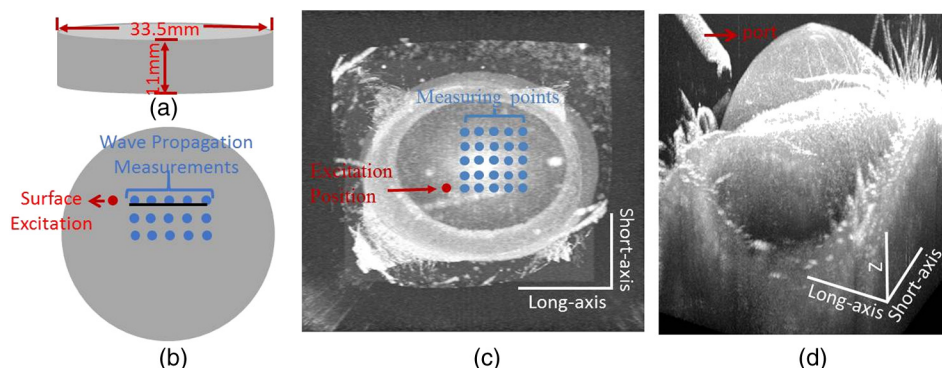


Fig. 2 Phantom sample is shown as (a). Excitation and measurement locations on (b) gelatin phantom and (c) mouse cornea *in vivo*. (d) shows the port and the mouse cornea. In (c) and (d), the scale along the long-axis is 4.8 mm, and for the short-axis, the scale is 4.4 mm, and for z , the scale is 2.2 mm.

A custom-made silicone model of an eye was also used in our study. This model provides an anterior surface scaled to match the curvature and size of the human eye. However, it has homogeneous optical and mechanical properties. The eye-mimicking model's anterior surface had a radius of curvature of 7.8 mm.

In vivo studies were performed on the corneas of three mice (15 to 22 months old). The cornea was kept hydrated by the periodical application of 0.9% saline solution during experiments. All animal manipulation procedures were approved by the Animal Care and Use Committee of the University of Houston.

Surface waves were excited with the air pressure set as ~ 10 Pa for the gelatin phantoms and silicone eye model, ~ 2.2 Pa for the contact lens, and ~ 5.9 Pa for mouse cornea *in vivo*. During all experiments, the distances between the tip of the air-pulse system port and the sample surface were kept within 0.3 mm, and time-dependent phase response was recorded from the surface of samples. Our investigation has shown that the air pressure of the system output remains relatively stable with the distance change within 10 mm between the port tip and the sample surface.³⁸ M-mode imaging over time at different positions (M-B scan mode) was utilized for OCT measurement. The spatial distributions of the excitation points and measurement points on the samples are shown in Fig. 2. The distance between the excitation point and the first measurement point was kept at more than 1 mm. The distance between two recording positions was 1 mm during the gelatin phantom, contact lens, and silicone eye model studies and 0.3 mm during *in vivo* studies.

2.3 Quantification Methods

To calculate amplitude of the surface waves from phase measurements, the following equation was used:³⁰

$$\text{Amplitude} = \frac{\lambda}{2\pi} \times \text{phase}, \quad (1)$$

where λ is the central wavelength of the OCT system.

The velocity of the elastic wave c was calculated as

$$c = \frac{d}{t}, \quad (2)$$

where d is the distance between the measurement points; t is the time delay of the elastic waves at two measurement positions. The main peak (peak with the highest amplitude) of deformation

was used to calculate the time delay. The time delay was defined as the difference between the time of the onset of air pulse and the time of surface wave arrival measured at the main peak. The distances between all adjacent points were 1 mm, and the calculations were based on each pair of adjacent points. Therefore, the velocity was calculated as 1 mm divided by the time delay difference between the two adjacent points.

Assuming that the phantoms are isotropic homogeneous elastic materials, the Young's modulus E of the sample can be calculated based on the wave velocity c as follows:³⁹

$$E = 2\rho(1 + \nu) \cdot \left[\frac{c \cdot (1 + \nu)}{0.87 + 1.12\nu} \right]^2, \quad (3)$$

where ρ is the mass density and ν is the Poisson's ratio of the medium. Although this equation was derived for a half-space, we used it as a first-order approximation to evaluate Young's modulus of the gelatin phantoms based on the group velocity of the surface waves measured in the experiment.

For the studies on contact lens, silicone eye model, and *in vivo* mouse cornea, the time delay was calculated relative to the position that is the nearest to the estimated excitation point and two-dimensional (2-D) rendered maps of time delay were generated.

3 Results and Discussion

3.1 Gelatin Phantom Studies

Figure 3(a) shows typical amplitude of the surface waves propagating in the 14% gelatin phantom recorded at various measurement locations away from the excitation position. These data clearly demonstrate that the amplitude decreases and the time delay increases with the increasing distance. Although the spatial-temporal profile of the air pulse is well characterized as a Gaussian pulse, it was not delivered perfectly normal to the specimen surface (mostly due to the geometrical coupling with the OCT imaging lens). It is possible that the angular separation of the air pulse and the measurement axis (~ 30 deg in this experiment) may influence the shape and force of the stimulus, thereby producing additional frequencies [the small amplitude vibration before the major deformation, as seen in Fig 3(a)]. Figure 3(b) shows the velocity of the surface waves measured in gelatin phantoms of different concentrations. The data indicate that the wave velocity increases with increasing concentration of gelatin, corresponding to the increase in the sample stiffness, which is consistent with our previous study.³⁰ The typical

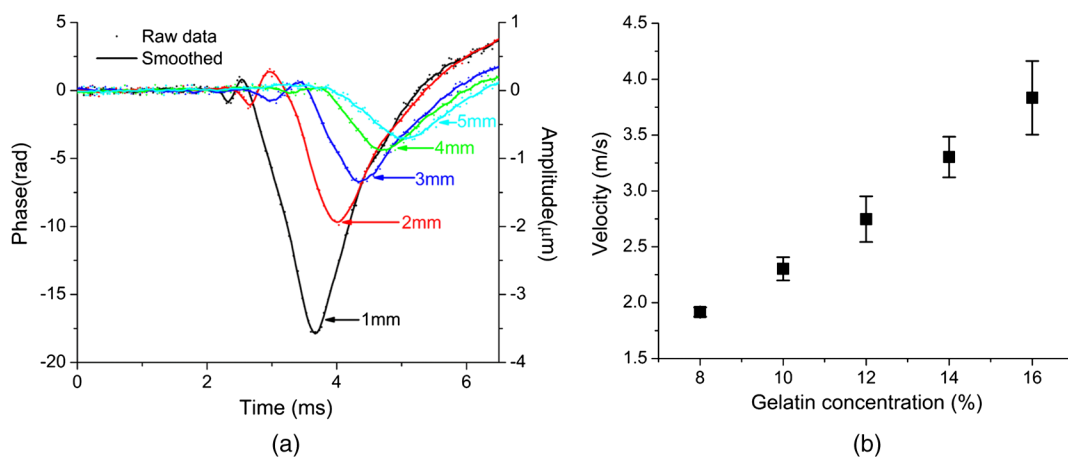


Fig. 3 (a) Phase responses recorded at various measurement points away from the source of excitation in 14% gelatin phantom. (b) The wave velocity as a function of the concentration of gelatin ($n = 9$).

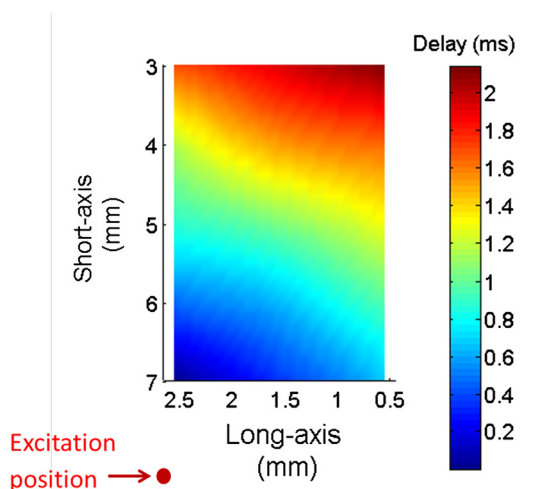


Fig. 4 Typical delay map measured in 12% gelatin phantom.

delay map of the 12% gelatin phantom is shown in Fig. 4, which also indicates that the time delay increased with the increasing of the distance.

The obtained Young's moduli of the gelatin phantoms are presented in Fig. 5. For the quantification, the density (ρ) of gelatin phantoms was assumed to be 1000 kg/m^3 and the Poisson's ratio (ν) of 0.5 was used to obtain E from Eq. (3).⁴⁰ The calculated Young's moduli of 8%, 10%, 12%, 14% and 16% gelatin phantoms are $12.2 \pm 0.6 \text{ kPa}$, $17.5 \pm 1.6 \text{ kPa}$, $25.1 \pm 3.8 \text{ kPa}$, $36.1 \pm 4.0 \text{ kPa}$, and $48.8 \pm 8.2 \text{ kPa}$, respectively. Additionally, a uniaxial testing system (In-Spec 2200, Instron, Inc., Northwood, Massachusetts) was used to measure the Young's moduli of gelatin phantoms with the same concentrations (Fig. 5). It can be easily seen that the estimated Young's moduli obtained from the wave velocity using OCT are reasonably close to those obtained using the uniaxial testing system. The small differences may be attributed to the fact that different samples were used in these two measurement methodologies (OCT measurements versus uniaxial testing).

3.2 Contact Lens Study

The experiment with a contact lens was performed with 0.9% saline solution placed between the contact lens and the

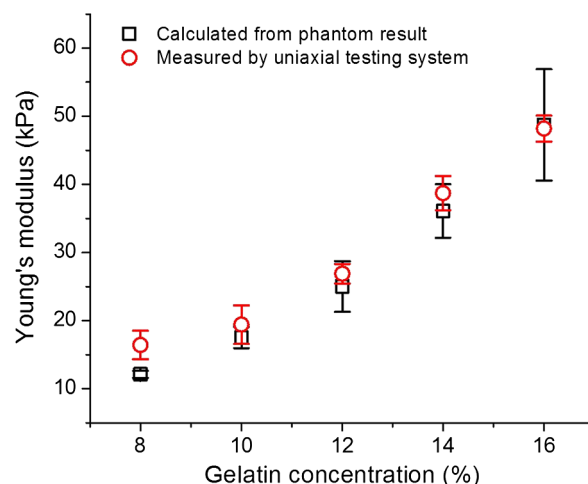


Fig. 5 Young's moduli of gelatin phantoms calculated from wave velocity and measured by the uniaxial testing system.

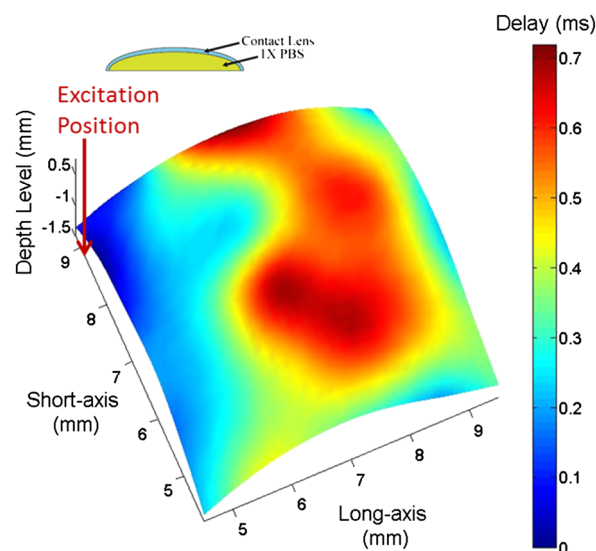


Fig. 6 2-D rendered map showing the time delay distribution on the surface of contact lens with 0.9% saline beneath the lens.

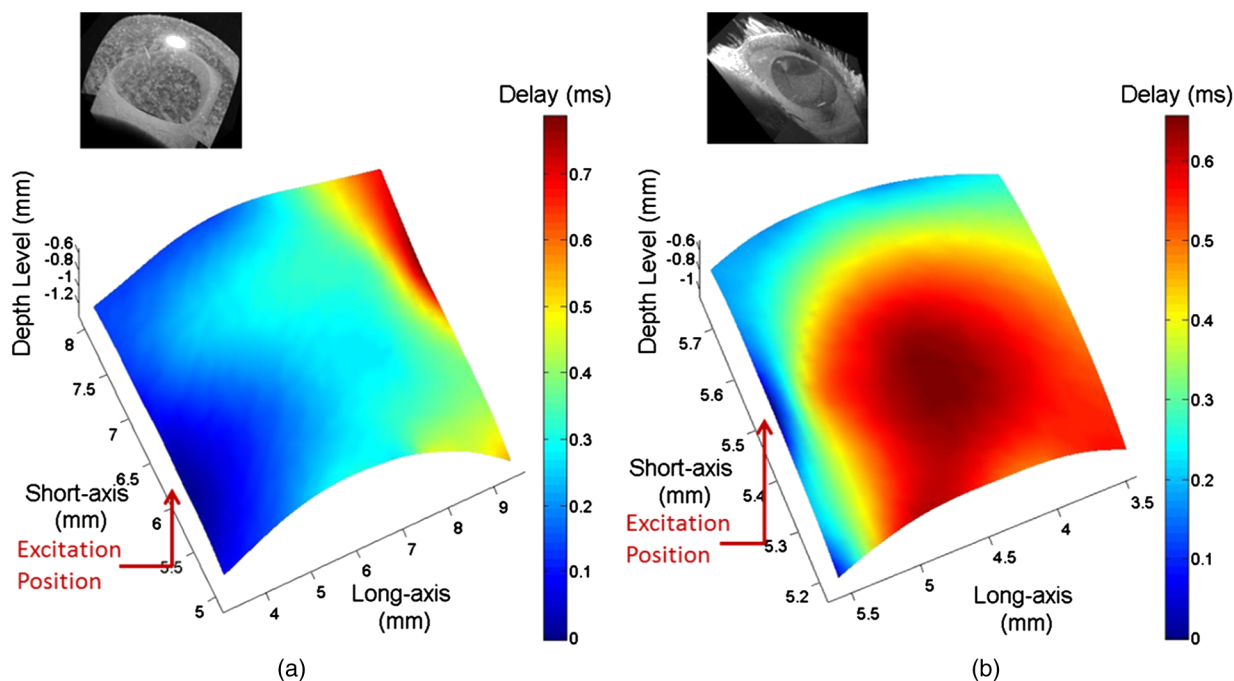


Fig. 7 (a) The measured time delay of elastic waves on (a) silicone phantom eye model and (b) 18-month-old mouse cornea *in vivo*.

supporting plate. Figure 6 shows the 2-D rendered map of time delay of the elastic waves in the contact lens. The result in Fig. 6 shows that the delay increases within greater distance in the contact lens and then decreases with the further increase in the distance.

There are several possible explanations for the observed difference in the delay distribution in phantoms and in the contact lens. One possibility is that the presence of the liquid on the lens posterior surface and the geometry of the lens produce a difference in how the energy propagates within the medium. For instance, the pressure pulse generates P-waves or compression waves that propagate much faster in the saline solution with low attenuation than the elastic waves in the cornea or lens material. As a result, these waves could produce additional sources of mechanical excitation in the lens after reflection from the hard surface. Therefore, the complex time delay distribution in the contact lens could be explained by the interaction of the different types of the waves. It is clear, however, that the presence of the liquid on the lens posterior surface complicates the wave pattern similar to what we observed in *in vivo* studies (see Fig. 7).

3.3 Silicone Eye Model and In Vivo Study of 18-Month-Old Mouse Cornea

Figures 7(a) and 7(b) show the OCT structural images and 2-D rendered maps for the time delay of the elastic waves measured in the silicone eye model and the mouse cornea *in vivo*, respectively. In Fig. 7(a), the time delay of the elastic wave increases as distance increases across the thick and homogeneous silicon layer that is different from what is observed in the real mouse eye. In Fig. 7(b), similar results as in Fig. 6 can be observed: the time delay of elastic waves increases with the increasing distance before reaching the corneal apex but decreases with greater distance after crossing the apex.

The distribution of time delay before the elastic waves that reach the apex can be used to quantify the wave velocity. For the

18-month-old mouse cornea, the velocity of the elastic wave is calculated as 0.92 to 7.42 m/s at different lateral positions due to heterogeneity of the tissue, which are potentially useful for the estimation of cornea elasticity. Additional work is required to develop a quantitative model to estimate corneal elasticity and to obtain corneal elastography because corneal tissue is inhomogeneous in both structure and composition. Equation 3, used here for isotropic homogenous materials, may not be proper to be used for the tissues like the cornea, which are composed of multiple layers and have curved surfaces.

This method does not involve tools that disrupt tissue or physically contact the eye. The displacement caused by air-pulse excitation on the cornea in these experiments is on the order of micrometers, which is much smaller than the indentation produced by the air puff used in clinical measurement of intraocular pressure (tonometry). Therefore, this approach is less invasive than current clinical procedures and suitable for delicate tissues or other sensitive materials. The high sensitivity of the PhS-SSOCT system enables accurate detection of the displacement of the cornea. These advantages allow the dynamic assessment of elastic waves propagating in ocular tissues and make it possible to estimate their biomechanical properties *in vivo*.

4 Conclusion

In this article, we have demonstrated that PhS-SSOCT can be used to monitor and assess the elastic waves that are induced by a focused air-pulse stimulus in tissue-mimicking phantoms, contact lenses, a silicone eye model, and the mouse cornea *in vivo*. For the phantoms, Young's modulus can be estimated based on the surface wave velocity. For the ocular models and tissue samples evaluated here, 2-D rendered maps of time delay caused by the propagation of elastic waves can be plotted. With further development, this noncontact optical method can be used to study the stiffness of delicate tissues such as the cornea and sclera of the eye. We also plan to

take into account a finite thickness of the cornea and its viscous properties. The current design of the system only permits experimental studies *in vivo* on animal models. For clinical studies, the distance between the port and the cornea will need to be properly secured and the first prototype is currently under construction.

Acknowledgments

This study was supported in part by NIH/NEI grants 1R01EY022362, P30EY07551.

References

- J. W. Ruberti, R. A. Sinha, and C. J. Roberts, "Corneal biomechanics and biomaterials," *Annu. Rev. Biomed. Eng.* **13**(1), 269–295 (2011).
- M. D. Roberts et al., "Correlation between local stress and strain and lamina cribrosa connective tissue volume fraction in normal monkey eyes," *Invest. Ophthalmol. Visual Sci.* **51**(1), 295–307 (2010).
- M. C. Chirambo and D. Benezra, "Causes of blindness among students in blind school institutions in a developing country," *Br. J. Ophthalmol.* **60**(9), 665–668 (1976).
- K. W. Hollman et al., "Strain imaging of corneal tissue with an ultrasound elasticity microscope," *Cornea* **21**(1), 68–73 (2002).
- D. V. Litwiller et al., "MR elastography of the ex vivo bovine globe," *J. Magn. Reson. Imaging* **32**(1), 44–51 (2010).
- M. Tanter et al., "High-resolution quantitative imaging of cornea elasticity using supersonic shear imaging," *IEEE Trans. Med. Imaging* **28**(12), 1881–1893 (2009).
- C. Li, Z. Huang, and R. K. Wang, "Elastic properties of soft tissue-mimicking phantoms assessed by combined use of laser ultrasonics and low coherence interferometry," *Opt. Express* **19**(11), 10153–10163 (2011).
- A. Manduca et al., "Magnetic resonance elastography: non-invasive mapping of tissue elasticity," *Med. Image Anal.* **5**(4), 237–254 (2001).
- P. J. McCracken et al., "Mechanical transient-based magnetic resonance elastography," *Magn. Reson. Med.* **53**(3), 628–639 (2005).
- R. Muthupillai et al., "Magnetic resonance elastography by direct visualization of propagating acoustic strain waves," *Science* **269**(5232), 1854–1857 (1995).
- J. Ophir et al., "Elastography: ultrasonic estimation and imaging of the elastic properties of tissues," *Proc. Inst. Mech. Eng. H* **213**(3), 203–233 (1999).
- K. J. Parker and R. M. Lerner, "Sonoelasticity of organs: shear waves ring a bell," *J. Ultrasound Med.* **11**(8), 387–392 (1992).
- M. D'Onofrio, A. Gallotti, and R. P. Mucelli, "Tissue quantification with acoustic radiation force impulse imaging: measurement repeatability and normal values in the healthy liver," *Am. J. Roentgenol.* **195**(1), 132–136 (2010).
- K. Nightingale, "Acoustic radiation force impulse (ARFI) imaging: a review," *Curr. Med. Imaging Rev.* **7**(4), 328–339 (2011).
- G. Grabner et al., "Dynamic corneal imaging," *J. Cataract Refractive Surg.* **31**(1), 163–174 (2005).
- X. Zhang and J. F. Greenleaf, "Estimation of tissue's elasticity with surface wave speed," *J. Acoust. Soc. Am.* **122**(5), 2522–2525 (2007).
- M. Tanter et al., "Quantitative assessment of breast lesion viscoelasticity: initial clinical results using supersonic shear imaging," *Ultrasound Med. Biol.* **34**(9), 1373–1386 (2008).
- K. D. Mohan and A. L. Oldenburg, "Elastography of soft materials and tissues by holographic imaging of surface acoustic waves," *Opt. Express* **20**(17), 18887–18897 (2012).
- G. Scarcelli and S. H. Yun, "In vivo Brillouin optical microscopy of the human eye," *Opt. Express* **20**(8), 9197–9202 (2012).
- G. Scarcelli, P. Kim, and S. H. Yun, "In vivo measurement of age-related stiffening in the crystalline lens by Brillouin optical microscopy," *Biophys. J.* **101**(6), 1539–1545 (2011).
- A. Kotecha, "What biomechanical properties of the cornea are relevant for the clinician?," *Surv. Ophthalmol.* **52**(6), S109–S114 (2007).
- G. J. Orsengo and D. C. Pye, "Determination of the true intraocular pressure and modulus of elasticity of the human cornea in vivo," *Bull. Math. Biol.* **61**(3), 551–572 (1999).
- A. Saad et al., "Biomechanical properties of keratoconus suspect eyes," *Invest. Ophthalmol. Visual Sci.* **51**(6), 2912–2916 (2010).
- C. Sun, B. Standish, and V. X. Yang, "Optical coherence elastography: current status and future applications," *J. Biomed. Opt.* **16**(4), 043001 (2011).
- X. Liang, V. Crecea, and S. A. Boppart, "Dynamic optical coherence elastography: a review," *J. Innov. Opt. Health Sci.* **3**(4), 221–233 (2010).
- M. H. De la Torre-Ibarra, P. D. Ruiz, and J. M. Huntley, "Double-shot depth-resolved displacement field measurement using phase-contrast spectral optical coherence tomography," *Opt. Express* **14**(21), 9643–9656 (2006).
- S. Wang et al., "Noncontact measurement of elasticity for the detection of soft tissue tumors using phase-sensitive optical coherence tomography combined with a focused air puff system," *Opt. Lett.* **37**(24), 5184–5186 (2012).
- C. Li et al., "Quantitative elastography provided by surface acoustic waves measured by phase-sensitive optical coherence tomography," *Opt. Lett.* **37**(4), 722–724 (2012).
- R. K. Manapuram et al., "In vivo estimation of shear wave parameters using phase stabilized swept source optical coherence elastography," *J. Biomed. Opt.* **17**(10), 100501 (2012).
- R. K. Manapuram et al., "Estimation of shear wave velocity in gelatin phantoms utilizing PhS-SSOCT," *Laser Phys.* **22**(9), 1439–1444 (2012).
- R. K. Manapuram et al., "Estimation of surface wave propagation in mouse cornea," *Proc. SPIE* **8209**, 82090S (2012).
- R. K. Manapuram et al., "3D assessment of mechanical wave propagation in the crystalline eye lens using PhS-SSOCT," *Proc. SPIE* **7885**, 78851V (2012).
- X. Liang et al., "Acoustomotive optical coherence elastography for measuring material mechanical properties," *Opt. Lett.* **34**(19), 2894–2896 (2009).
- M. Razani et al., "Feasibility of optical coherence elastography measurements of shear wave propagation in homogeneous tissue equivalent phantoms," *Biomed. Opt. Express* **3**(5), 972–980 (2012).
- R. K. Manapuram, V. G. R. Manne, and K. V. Larin, "Phase-sensitive swept source optical coherence tomography for imaging and quantifying of microbubbles in clear and scattering media," *J. Appl. Phys.* **105**(10), 102040–102049 (2009).
- R. K. Manapuram, V. G. R. Manne, and K. V. Larin, "Development of phase-stabilized swept-source OCT for ultra-sensitive quantification of microbubbles," *Laser Phys.* **18**(9), 1080–1086 (2008).
- T. J. Hall et al., "Phantom materials for elastography," *IEEE Trans. Ultrasonics Ferroelectrics Freq. Control* **44**(6), 1355–1365 (1997).
- S. Wang et al., "A focused air-pulse system for optical coherence tomography-based measurements of tissue elasticity," *Laser Phys. Lett.* **10**(7), 075605 (2013).
- J. F. Doyle, *Wave Propagation in Structures: Spectral Analysis Using Fast Discrete Fourier Transform*, Springer-Verlag, New York (1997).
- X. Zhang, B. Qiang, and J. Greenleaf, "Comparison of the surface wave method and the indentation method for measuring the elasticity of gelatin phantoms of different concentrations," *Ultrasonics* **51**(2), 157–164 (2011).